Available online at www.sciencedirect.com
SCIENCE DIRECT®
Journal of Power Sources 147 (2005) 85–94
JOURNAL OF POWER SOURCES
www.elsevier.com/locate/jpowsour

Design considerations for segmented-in-series fuel cells

Tammy S. Lai, Scott A. Barnett *

Materials Science and Engineering Department, Northwestern University, 2220 Campus Dr., Evanston, IL 60208, USA

Received 19 November 2004; accepted 6 January 2005
Available online 21 February 2005

Abstract

This paper describes calculations of the electrical losses in patterned series-connected solid oxide fuel cells (SOFCs), i.e. the "segmented-in-series" configuration. Losses due to cell resistances, electrode ohmic resistances, interconnect resistance, and shunting by a weakly-conductive support material were considered. For any given set of cell dimensions and characteristics, power density was maximized at an optimal cell length – the power decreased at larger cell lengths due to electrode lateral resistance loss and decreased at smaller cell lengths due to a decreasing fraction of cell active area. For cell lengths well above the optimal value, electrolyte current was often confined to the portion of the cell nearest to where the less conductive electrode (i.e. the cathode) connected to the interconnect. Assuming dimensions expected for screen printing, i.e. ≈20 μm thick electrodes and lateral print accuracy of ≈100 μm, and area specific resistance values typical of SOFCs, optimal cell lengths typically ranged from 1 to 3 mm. Shunting currents increased with decreasing cell lengths, but were found to have little effect on power density assuming partially-stabilized zirconia supports and temperatures ≤ 800 °C.

Keywords: SOFC; Modeling; Segmented-in-series; Shunting current; Optimization

1. Introduction

The "segmented-in-series" solid oxide fuel cell (SS-SOFC) design has often been implemented in a tubular configuration, with the cells delineated in bands around the tube, leading to the term "banded tubular" [1]. Fig. 1 shows schematically a cross-sectional view of this geometry. Recently, a similar design using flattened tubes instead of circular tubes has also been reported [2]. Cell lengths were typically ≥ 10 mm in both circular and flattened tube designs. In addition to the general advantages of tubes – seals are not required, and the interconnect is an integral layer rather than a separate piece – flattened tubes allow for higher packing density, thereby yielding higher power-to-volume ratios and facilitating the use of low-cost planar deposition methods such as screen printing.

General predictions regarding the performance of SS-SOFCs have been made based on modeling of the electrical, electrochemical, heat and mass transfer processes [3]. In a recent paper, we suggested that SS-SOFCs could provide improved performance if the cell lengths were decreased below 10 mm, and demonstrated the fabrication of 1–2 mm long cells by screen printing [4]. A simple calculation also showed that the increased number of interconnects, due to the larger number of cells per unit length, should not be detrimental to performance. An estimate of the support shunting current was also given. However, neither of these papers considered in detail the limitations on SS-SOFC geometries imposed by practical processing methods, or made predictions concerning the optimal geometries and their expected performance.

In this paper, we present quantitative performance predictions for SS-SOFCs as a function of cell and interconnect geometry, support material, cell area-specific resistance, and electrode sheet resistance. Most of the calculations were done assuming ceramic layer fabrication by screen printing, where the minimum feature size is ≈100 μm. The results provide guidance regarding optimal SS-SOFC geometries and their expected power densities.

* Corresponding author. Tel.: +1 847 491 2447; fax: +1 847 491 7820.
E-mail address: s-barnett@northwestern.edu (S.A. Barnett).

0378-7753/$ – see front matter © 2005 Elsevier B.V. All rights reserved.
doi:10.1016/j.jpowsour.2005.01.002

2. Calculation methods

Two main calculations were carried out. First, the electrode resistance losses across segmented-in-series cells and interconnects were calculated. Second, the shunting current between cells across the support was calculated. Cell dimensions were chosen to reflect the capabilities of screen printing, a commonly used SOFC fabrication method. In terms of lateral print resolution, all lines and spaces were chosen to be at least 0.1 mm to reflect what is achievable with typical screen mesh counts (230 and 325), as well as visual pattern alignment. Layer thicknesses were also chosen to approximate typical results from printing with 230 or 325 mesh screens: a single printed layer is usually 15–20 μm, while a double printed layer (dried between printings) is 30–40 μm thick.

2.1. Resistance loss calculation

The overall resistance of an array of identical cells, illustrated in Fig. 1, was obtained by calculating the resistance of an individual repeat period (Λ) and multiplying by the number of cells. Component resistances R were calculated, for the most part, based on $R = \rho l_{path}/A$, where ρ is the component resistivity, l_{path} is the length of the current path, and A is the cross sectional area. The exception to this was the cell resistance R_{CELL}, in the portion of the device in Fig. 1a, where the calculation is complicated by the variation in cell current density with lateral position (x). The total resistance for each repeat unit (of length Λ) also included electrode length in the gap between the active cell area and the interconnect, such that:

$$R_\Lambda = R_{CELL} + \frac{\rho_{ca}(L_{G,an} + (L_I/2))}{t_{ca} w} + \frac{\rho_{an}(L_{G,ca} + (L_I/2))}{t_{an} w} + \frac{\rho_I t_I}{L_I w} \quad (1)$$

where the dimensions are as given in Fig. 1b, ρ_{ca} is the cathode resistivity, ρ_{an} is the anode resistivity, ρ_I is the interconnect resistivity, and w is the cell width (into the plane of Fig. 1). The interconnect length was assumed small and the electrode resistivities were assumed small enough that the current density across the interconnect was uniform, allowing the use of the simple interconnect term in Eq. (1). The anode and cathode gap resistance terms were approximated simply by including half of the interconnect length in the electrode current paths. This does not introduce substantial error, given that this resistance is small relative to the other terms in Eq. (1). Maximum power density (MPD) was calculated using (MPD) $= 0.55^2/R_\Lambda \Lambda w$ where an open circuit voltage of 1.1 V was assumed.

The calculation of R_{CELL} accounted for the anode current decrease and the cathode current increase due to current traversing the electrolyte (Fig. 1a). The equations describing the current flow and voltage drops are given in Eqs. (2)–(4). The parameters are defined in Appendix A.

$$dI_{an} = -dI_{ca} = -J_{el} L_{CELL}\, dx = -\frac{V_{OC} - (V_{ca} - V_{an})}{R_{ca/el} + R_{an/el} + R_{el}} L_{CELL}\, dx \quad (2)$$

$$dV_{an} = -I_{an} R = -I_{an} \frac{\rho_{an}}{L_{CELL}\, t_{an}} dx \quad (3)$$

$$dV_{ca} = -I_{ca} R = -I_{ca} \frac{\rho_{ca}}{L_{CELL}\, t_{ca}} dx \quad (4)$$

Integration of these equations was performed in Matlab [5] by a simple iterative technique. The initial calculation began at $x = 0$ with the values $I_{ca}(x = 0)$ and $V_{an}(x = 0)$ set to 0, cell current (I_{CELL}) set to $I_{an}(x = 0)$, and a trial value of $V_{ca}(x = 0)$ chosen. Eq. (2) gives $dI_{an} = -dI_{ca}$, calculated as the current flow across the electrolyte between x and $x + dx$. For simplicity, the polarization resistances $R_{ca/el}$ and $R_{an/el}$ were assumed to be ohmic. Eqs. (3) and (4) give the voltage drops from x to $x + dx$ for the anode dV_{an} and cathode dV_{ca}, respectively. $V_{ca}(x = 0)$ was iteratively varied using a bisection algorithm until the boundary condition that $I_{an}(x = L_{CELL}) = 0$ was satisfied. Calculations with different length increments dx were done and the results compared to ensure convergence to the

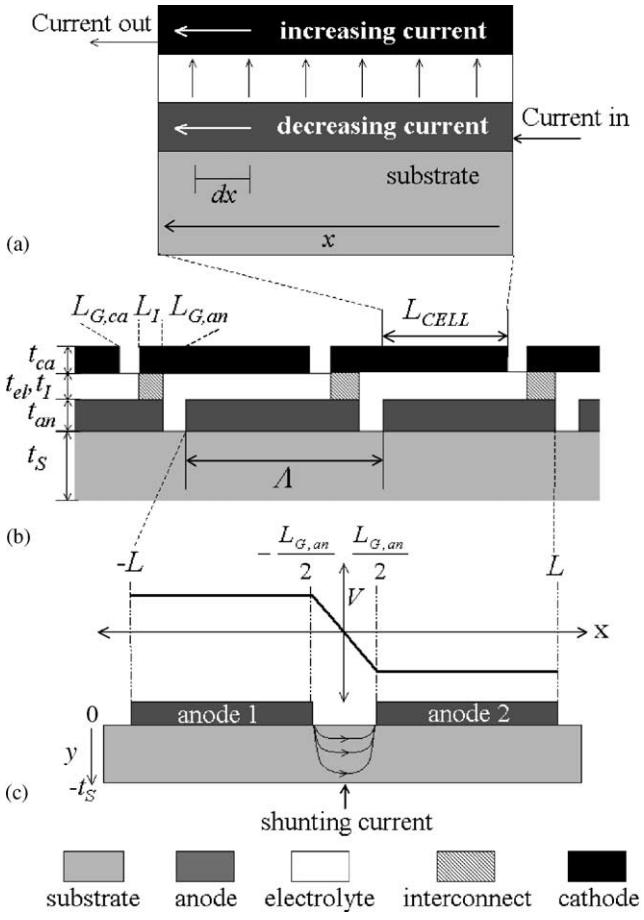

Fig. 1. Cross sectional schematics of the SS-SOFC. Part (a) shows an individual cell with current flows indicated. Part (b) shows an overall view with dimensions labeled. Part (c) shows a closeup view of the shunting current calculation. Note: drawings are not to scale.

same value. The resulting values were used to give the resistance $R_{CELL} = V_{ca}(x = L_{CELL})/I_{CELL}$ in Eq. (1). The cell's operating voltage is defined as the difference between the cathode potential at $x = L_{CELL}$ and the anode potential at $x = 0$, $V_{an}(x = 0) = 0$, such that $V_{CELL} = V_{ca}(x = L_{CELL})$.

As a check of the present numerical calculation, total resistance values were compared with those obtained from the analytical expression given in Ref. [3], and the agreement was very good.

2.2. Shunting current calculation

This section describes the calculation of the current flowing between cells through a mildly conductive support, as illustrated in Fig. 1c. The goal was to provide a more accurate result than in previous work [4], where the crude assumption of a uniform field across the support was employed. Fig. 1c shows a cross sectional schematic of two cells along with the assumed potential versus lateral position at the surface of the support ($y = 0$). Since a typical Ni–YSZ anode is quite conductive, the potential gradient is entirely across the gap between anodes:

$$V(x) = -\frac{V_o}{2} \quad \text{for} \quad -L \le x \le -\frac{L_{G,an}}{2} \tag{5}$$

$$V(x) = \frac{V_o}{L_{G,an}}x \quad \text{for} \quad -\frac{L_{G,an}}{2} \le x \le \frac{L_{G,an}}{2} \tag{6}$$

$$V(x) = \frac{V_o}{2} \quad \text{for} \quad \frac{L_{G,an}}{2} \le x \le L \tag{7}$$

where V_o is the cell operating voltage. Since the potential was assumed not to vary in the z direction (perpendicular to the plane of the cross section pictured in Fig. 1c), it was approximated by a two-dimensional solution to Laplace's equation for a rectangular area [6]:

$$V(x, y) = \frac{A_o}{2} + \sum_n (A_n \cos \beta_n x + B_n \sin \beta_n x) \times (C_n e^{\beta_n y} + D_n e^{-\beta_n y}) \tag{8}$$

where the constants A_o, A_n, B_n, and β_n can be calculated using the case at $y = 0$ when $Y_n \equiv C_n e^{\beta_n y} + D_n e^{-\beta_n y} = 1$:

$$A_o = \frac{1}{L}\int_{-L}^{L} V(x)\mathrm{d}x \tag{9}$$

$$A_n = \frac{1}{L}\int_{-L}^{L} V(x)\cos \beta_n x \mathrm{d}x \tag{10}$$

$$B_n = \frac{1}{L}\int_{-L}^{L} V(x)\sin \beta_n x \mathrm{d}x \tag{11}$$

$$\beta_n = \frac{\pi n}{L} \tag{12}$$

In order to solve for the constants C_n and D_n, two boundary conditions were used:

$$\text{at} \quad y = 0, \; Y_n = 1 \tag{13}$$

$$\text{at} \quad y = -t_S, \; \frac{\mathrm{d}Y_n}{\mathrm{d}y} = 0 \tag{14}$$

The first boundary condition assures that potential profile will match Eqs. (5)–(7) at $y = 0$, while the latter condition expresses that no current can flow in the y direction at the free surface of the support. The calculation was carried out over four complete cells, and the potential variation taken between the central two cells in order to eliminate edge effects.

The expression for the potential profile was then differentiated, according to the expression

$$J = \frac{-\nabla V}{\rho_S} \tag{15}$$

in order to find the approximate current density between the two cells [7]. The expression is applicable to weakly-conductive ohmic materials with isotropic dielectric properties, where localized charges do not affect the potential gradient.

3. Results

3.1. Resistance loss calculation

In this section, the calculated voltage and current distributions across SS-SOFCs are described for two categories of cells where: (a) the cathode and anode sheet resistances are approximately equal, and (b) one electrode has a significantly smaller sheet resistance. More attention is given to this latter case, since it is a more common situation in actual SOFCs, in which the Ni-based anode is more conductive than the perovskite cathode. For Ni-based anodes a sheet resistance of 0.5 Ω/□ is used based on a thickness of 20 μm and a resistivity of ≈1×10^{-3} Ω cm [8], as previously reported for porous Ni–$(ZrO_2)_{0.92}(Y_2O_3)_{0.08}$ (Ni–YSZ) in a 55:45 volume ratio [4]. For perovskite cathode materials such as (La,Sr)MnO_3 (LSM), a sheet resistance of 10 Ω/□ is used, based on a resistivity of ≈0.02 Ω cm and a 20 μm layer thickness. For simplicity, the individual cells are assumed to follow ohmic behavior, and the cell area-specific resistance $R_{AS} = R_{ca/el} + R_{an/el} + R_{el}$ value was 0.5 Ω cm^2 unless otherwise specified.

3.1.1. Symmetrical electrode cell current variations

This section describes calculations done for the case where the electrode sheet resistances are equal. All electrode potential profiles and electrolyte current densities were calculated for cells operating at maximum power, i.e. with $V_{CELL} = V_{ca}(x = L_{CELL}) = 0.55$ V. Fig. 2 shows the potential (a) and electrolyte current density (b) versus position for 2 mm long cells, for sheet resistances of 0.5 or 10 Ω/□. For

the lower sheet resistance, the potential variation across each electrode was very small, with a nearly constant electrolyte current density, i.e. there were effectively no electrode resistance losses. For the higher sheet resistance, however, the potential drop was about 0.15 V across the 2 mm long cell for each electrode. The potential gradient is high in the anode and low in the cathode near $x = 0$, due to the much higher current in the anode. The situation is reversed near $x = L_{CELL}$, where most of the current is in the cathode. The electrolyte current density dropped to a minimum at the midpoint of the cell, where the electrode potential difference deviates the least from OCV.

Fig. 3 shows the results of a similar calculation done with 10 mm long cells. The results are qualitatively similar, but the larger electrode lengths lead to larger potential variations. The potential variation was especially large for the higher sheet resistance, ≈0.4 V across each electrode, corresponding to most of the cell potential drop of 0.55 V. The electrolyte current densities displayed more variation and were lower than in Fig. 2, especially for the larger sheet resistance where the current density dropped to near zero at the center

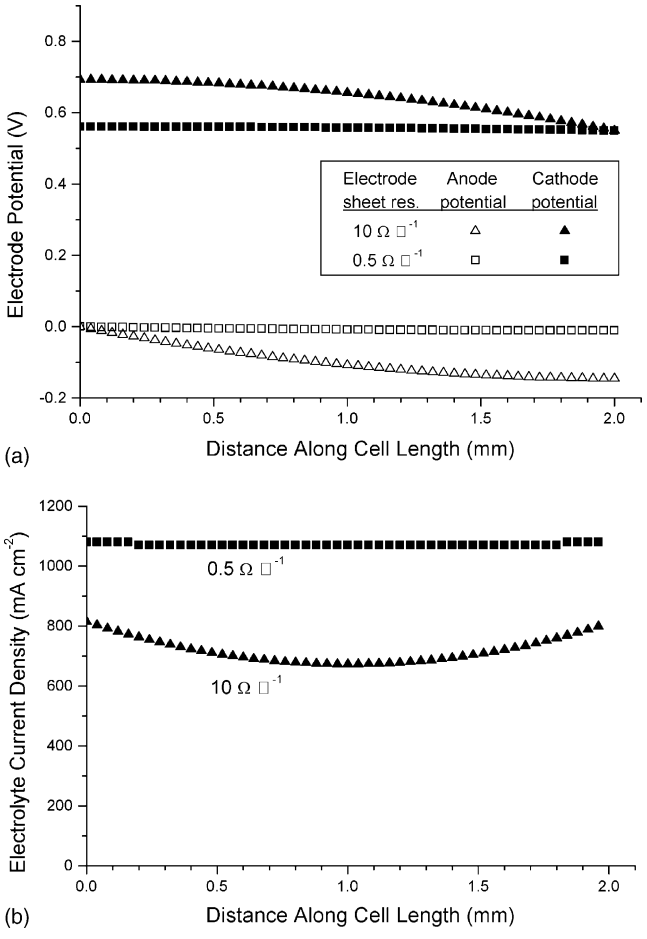

Fig. 2. Anode and cathode potential (a) and electrolyte current density (b) vs. position x for 2-mm-long symmetric-electrode cells, for sheet resistances of 0.5 or 10 Ω/□.

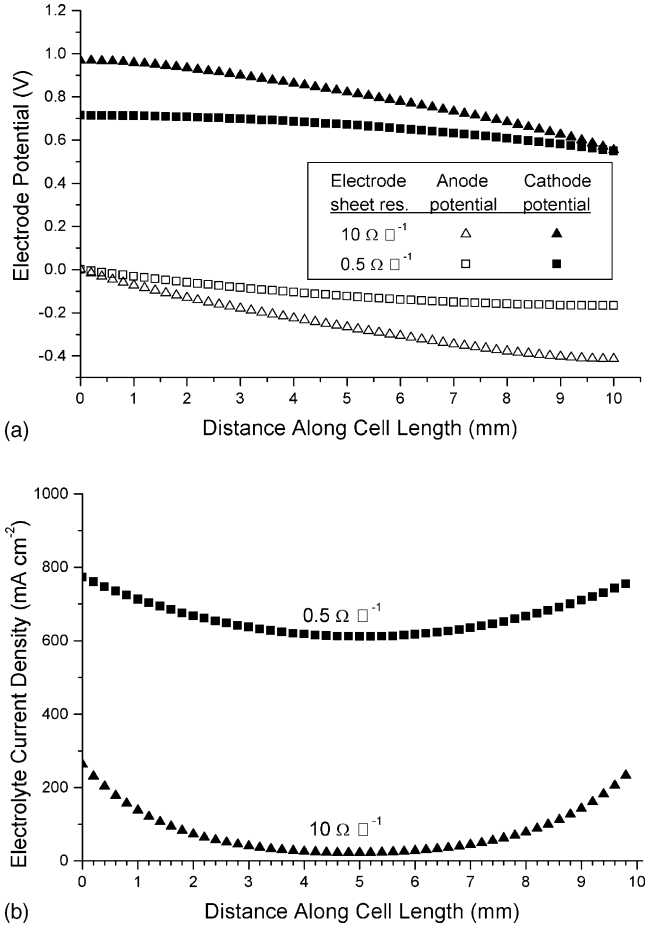

Fig. 3. Anode and cathode potential (a) and electrolyte current density (b) vs. position x for 10-mm-long symmetric-electrode cells, for sheet resistances of 0.5 or 10 Ω/□.

of the cell. These results show that higher sheet resistances require the use of smaller cell lengths to minimize ohmic losses.

3.1.2. Asymmetrical electrode cell current variations

These calculations were done for sheet resistance values of 0.5 Ω/□ for the anode (e.g. Ni–YSZ), with 10 Ω/□ or 30 Ω/□ for the cathode, the latter expected for ≈20 μm thick LSM or $La_{0.6}Sr_{0.4}Co_{0.2}Fe_{0.8}O_3$ (LSCF) layers taking porosity into consideration [9]. Fig. 4 illustrates the electrode potential (a) and electrolyte current density (b) versus position across a cell at maximum power output. The anode potential was essentially constant. The cathode potential did vary substantially with position. For the cathode sheet resistance of 30 Ω/□, the cathode potential dropped ≈0.3 V, as compared to ≈0.15 V for the lower cathode sheet resistance. As shown in Fig. 4b, the electrolyte current for the high sheet resistance case was smaller than the low resistance case near $x = 0$ mm, as expected because the voltage was closer to V_{OC} (Fig. 4a). The electrolyte current variation was larger for the higher cathode sheet resistance.

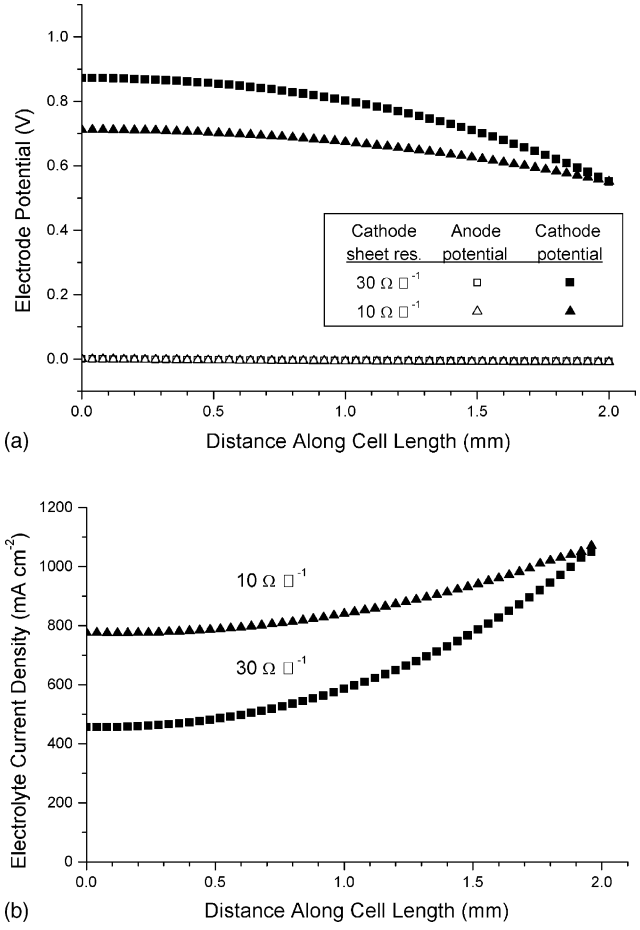

Fig. 4. Anode and cathode potential (a) and electrolyte current density (b) vs. position x for 2-mm-long asymmetric-electrode cells, for cathode sheet resistances of 10 or 30 Ω/□.

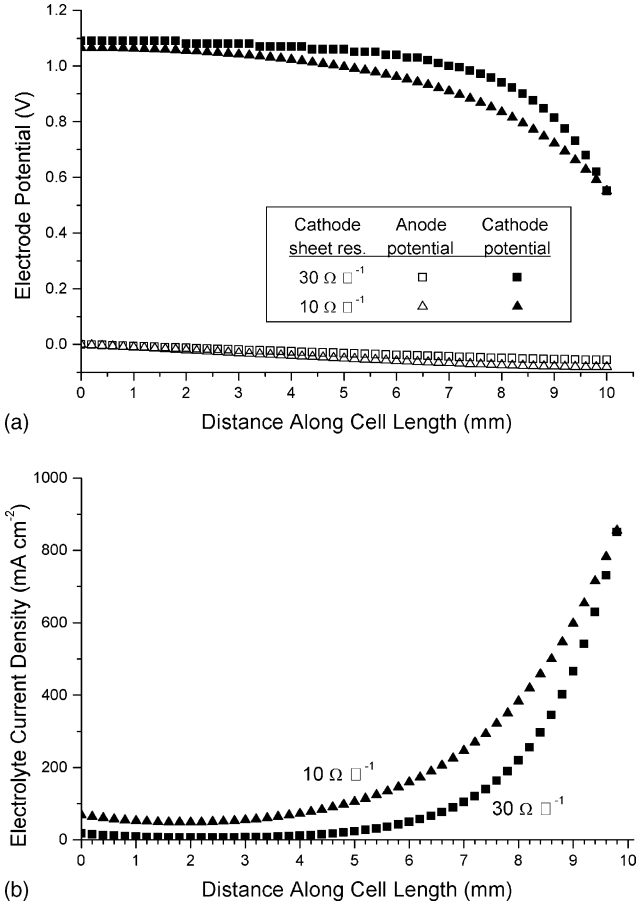

Fig. 5. Anode and cathode potential (a) and electrolyte current density (b) vs. position x for 10-mm-long asymmetric-electrode cells, for cathode sheet resistances of 10 or 30 Ω/□.

For comparison, the same calculation was carried out for L_{CELL} = 10 mm. Fig. 5 shows the electrode potentials (a) and electrolyte current density (b) versus length. The overall dependence is similar to that in Fig. 4, although the potential gradients and the increase in current density at large x are more pronounced. Most of the current travels through the anode and crosses the electrolyte at large x in order to avoid a long current path across the more resistive cathode. For the lower cathode sheet resistance, the electrolyte current initially decreases with increasing x, shows a weak minimum near x = 3 mm, and then increases. The initial decrease near x = 0 occurs because of a slight decrease in the local cell voltage, i.e. a decrease in anode potential while the cathode potential remains constant (Fig. 5a). The anode potential change occurs, despite the relatively low sheet resistance of the anode, because almost all of the cell current is in the anode at x = 0. There is little corresponding cathode potential change because little current is in the cathode. As x increases, more of the current transfers to the cathode, such that the cathode potential decreases rapidly. A comparison of Figs. 4b and 5b shows that the high cathode sheet resistance prevents substantial current flow except within ≈2 mm of the interconnect for both the 2 and 10 mm cells.

Fig. 6 summarizes results on electrolyte current density versus position for total cell lengths ranging from 1 to 10 mm. It is clear from this figure that smaller cell lengths resulted in more uniform current distributions and higher average elec-

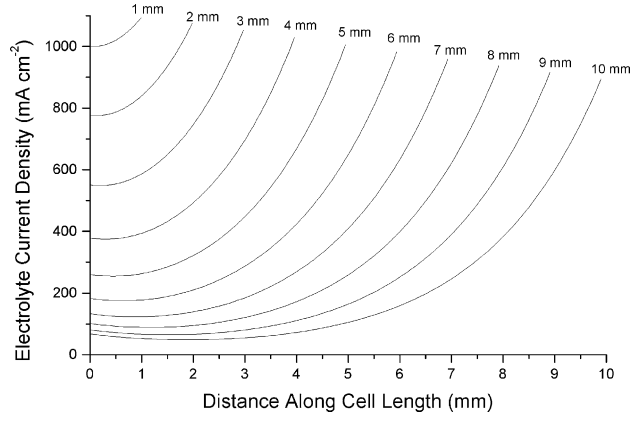

Fig. 6. Current density through the electrolyte for cell lengths from 1–10 mm. Calculations were based on cell operation at maximum power density, cathode sheet resistance of 10 Ω/□, and R_{AS} = 0.5 Ω/□.

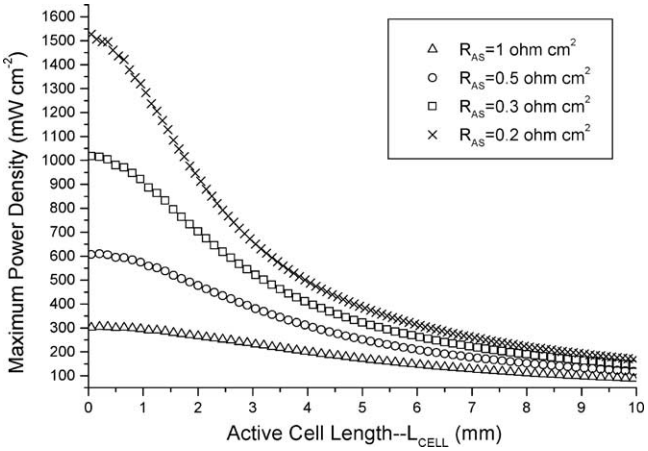

Fig. 7. Maximum power densities vs. cell length for various area specific resistances and cell lengths. Only active cell area was used and interconnect losses were not included in this power density calculation. The cathode sheet resistance was 10 Ω/□.

trolyte current densities, primarily due to the shorter electrode lateral current paths.

3.1.3. Performance of asymmetrical cells

In this section, we illustrate the impact of electrode resistance losses on overall performance. Fig. 7 shows the maximum power density (MPD) versus active cell length L_{CELL} for an anode sheet resistance of 0.5 Ω/□, a cathode sheet resistance of 10 Ω/□, and R_{AS} = 1.0, 0.5, 0.3, and 0.2 Ω cm^2. In this figure, power densities were calculated using only the active cell area. The greatest maximum power densities occurred at the smallest cell lengths, as expected given the results in the previous sections. Cell lengths of 10 mm resulted in much smaller power densities.

The calculation was extended to include losses due to the interconnect and inactive portions of the electrodes (Eq. (1)), and account for the full surface area of the array. Table 1 gives the values used in the calculations. Referring to Fig. 1, the surface can be divided into active cell length (L_{CELL}) and interconnect/gap length ($L_I + L_{G,an} + L_{G,ca}$). We have assumed interconnect/gap lengths that are fixed by processing considerations. For example, in screen printing, there are limitations on resolution and print-to-print alignment. Two cases are considered here. First, lengths were assumed that are relatively easy to achieve, i.e. $L_{G,an} = L_{G,ca} = L_I = 0.25$ mm. Second, we chose lengths near the limits of screen printing, i.e. $L_{G,an} = L_{G,ca} = L_I = 0.1$ mm.

Fig. 8 shows MPD curves for the two cases, each showing an optimal MPD for each R_{AS} value. Indicated in the figure are the values of L_{CELL} corresponding to the optimal MPDs. Also shown on these figures is the fraction of the surface that is active cell area. The MPD occurs at active area fractions from ≈0.5 to 0.8. The maximum is a result of the electrode resistance effect, shown in Fig. 7, combined with the decreasing fraction of active cell area with decreasing L_{CELL}. Maximum power densities were substantially lower than the maximum achievable shown in Fig. 7. Decreasing the gap/interconnect lengths allowed narrower cells while maintaining a reasonably high active cell fractional area. Thus, the maximum power densities were higher and optimal cell lengths smaller for the smaller gap/interconnect lengths shown in Fig. 8b. Note that for the smaller gap/interconnect lengths, the electrode lengths are decreased, decreasing that resistance, but the narrower interconnect has a higher resistance.

Table 1
Parameters used in maximum power density calculations

Parameter	Value
Anode sheet resistance	0.5 Ω/□
Cathode sheet resistance	10 Ω/□
Interconnect resistivity	1 Ω cm
Interconnect thickness	20 μm

Besides the cell length and R_{AS}, the other key factor affecting cell performance is the cathode sheet resistance. Since typical cathode material resistivities fall within a narrow range, the sheet resistance will be primarily varied via cathode thickness. Fig. 9 shows the MPD versus cell length for different cathode sheet resistances. Decreasing the sheet resistance allows good power densities to be maintained at higher cell lengths. For example, for a 10 mm cell with a 10 Ω/□ cathode sheet resistance (≈20 μm thick), the MPD is

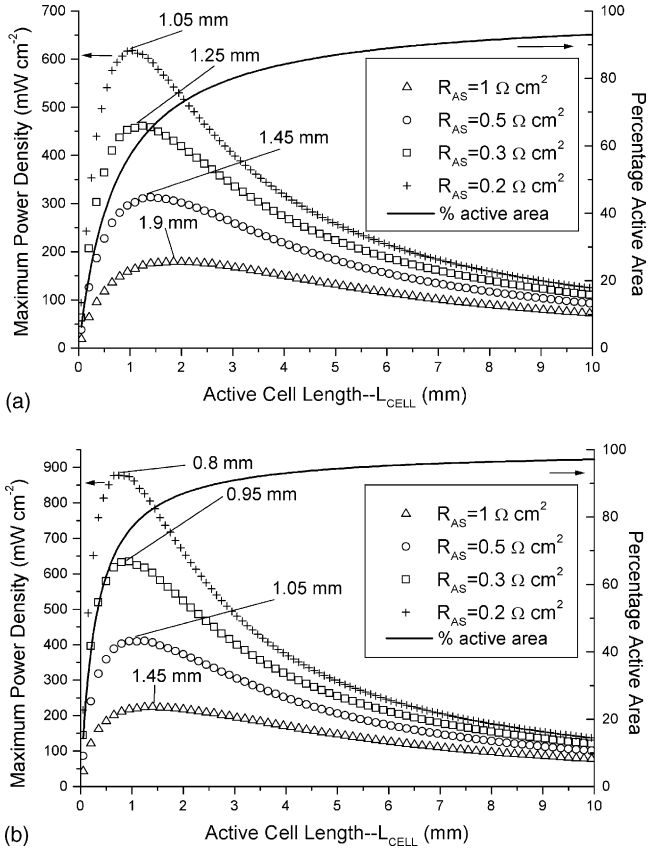

Fig. 8. Maximum power density, calculated including cell and interconnect area, for (a) $L_{G,an} = L_{G,ca} = L_I = 0.25$ mm and (b) $L_{G,an} = L_{G,ca} = L_I = 0.1$ mm using different values of R_{AS}. Also shown is the percent active area for each cell length.

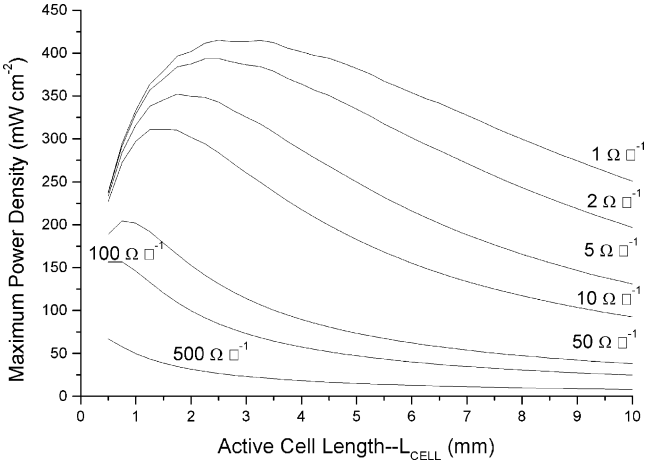

Fig. 9. Maximum power density, calculated including cell and interconnect area, as a function of active cell length for various cathode sheet resistances and $R_{AS} = 0.5\,\Omega\,cm^2$. The present screen printed cathode sheet resistance is ≈10 Ω/□.

only 118 mW cm^{-2}. Decreasing the sheet resistance to 1 Ω/□ (≈200 μm thick), the MPD is increased to 307 mW cm^{-2}. It should be noted that MPDs at a length of 10 mm are less than those of narrower cells, and that a processing technique other than screen printing would be required to make such thick cathode layers.

Resistance losses in the interconnect region can also influence overall cell performance. Because of the relatively high resistivity of typical ceramic interconnect materials, this can be an important effect. To demonstrate the effect of the interconnect length on array performance, the array's optimum MPD and the optimum active cell length are plotted versus interconnect length in Fig. 10. R_{AS} was assumed to be $0.5\,\Omega\,cm^2$ and the electrode gap lengths were kept constant at $L_{G,ca} = L_{G,an} = 0.25$ mm. With those parameters, an interconnect length of 0.1 mm and an associated active cell length of 1.35 mm gave the highest MPD. Larger interconnect lengths resulted in lower MPDs due to the smaller fraction of active cell area. Decreasing the length below 0.1 mm

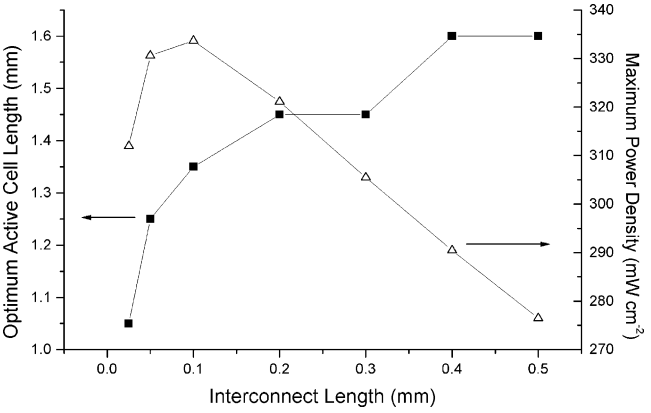

Fig. 10. Maximum power density and optimum active cell length vs. interconnect length for interconnect thickness of 20 μm and resistivity of 1 Ω cm.

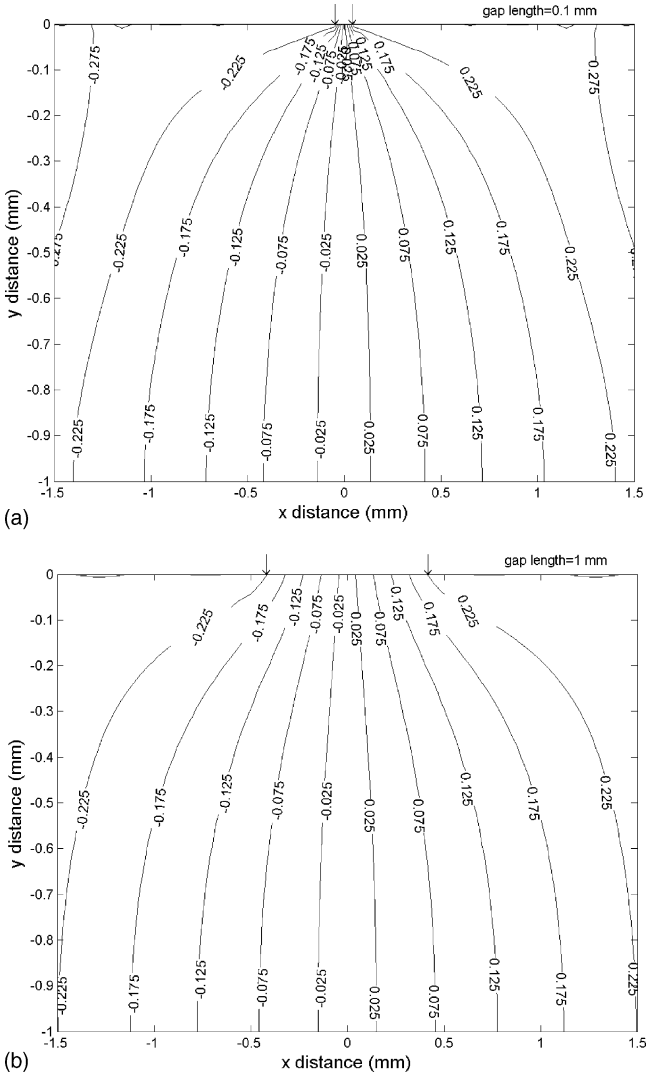

Fig. 11. Equipotential plots for gap lengths (a) 0.1 mm and (b) 1 mm. Gaps are bounded by arrows.

also lowered MPDs because of the increasing interconnect resistance.

3.2. Shunting current calculation

Fig. 11 shows examples of the calculated equipotential lines within the support for cells with $L_{CELL} = 2$ mm, support thickness $t_S = 1$ mm, and gap lengths $L_{G,an} = 0.1$ (a) and 1 mm (b). From Eq. (11), current flow is perpendicular to the equipotential lines, with magnitude proportional to the line density. Directly below each electrode, there were few equipotential lines and hence little current flow, as expected since the electrodes are at constant potential. Well below the electrode gap, the lines were generally uniformly spaced, indicating uniform current flow. Near the electrode gaps, the lines were more tightly spaced, indicating a higher current density. For the smaller gap, the lines were more tightly

bunched, indicating a higher field and current density localized in a smaller volume.

In order to provide an example of the shunting current expected in a typical SS-SOFC, we have assumed PSZ supports. Resistivity values for dense PSZ range from ≈1300–220 Ω cm between 575 and 1000 °C, respectively [10]. These values were corrected to account for the typical porosity of 30–40 vol.% [4]. Since PSZ is ionically conductive and the Ni–YSZ electrodes are electronically conductive, current flow through the support requires electrochemical reactions at each of the interfaces (Fig. 1c), resulting in an associated polarization resistance. This resistance is neglected in the present calculation since its value may vary greatly depending on exact electrode composition and structure. *Thus, the shunting current values given below must be regarded as upper limits*.

The net substrate current I_{shunt} was obtained by integrating the current in Eq. (15) over the thickness of the support at the midpoint between the two cells ($x = 0$ in Fig. 11):

$$I_{\text{shunt}} = \iint_{z,y} J(x=0)\mathrm{d}z\mathrm{d}y = \iint_{z,y} \left(\frac{-\nabla V(x=0)}{\rho_{\text{S}}}\right)\mathrm{d}z\mathrm{d}y$$

$$= -\left(\frac{w}{\rho_{\text{S}}}\right)\int_{y} \left.\frac{\mathrm{d}V}{\mathrm{d}x}\right|_{x=0}\mathrm{d}y \quad (16)$$

Note that since $\mathrm{d}V/\mathrm{d}y = \mathrm{d}V/\mathrm{d}z = 0$ at the midpoint by symmetry, $\nabla V = \mathrm{d}V/\mathrm{d}x$. We have plotted $I_{\text{shunt}}\rho_{\text{S}}/w$ in Fig. 12 as a function of $L_{\text{G,an}}$ for three different values of L_{CELL}: 1, 2, and 5 mm and a support thickness of 1 mm. The shunting current increased gradually with decreasing gap length. This can be explained from the equipotential plots in Fig. 11. While the equipotential lines far from the gap changed little with gap length, the lines became very closely spaced within the narrower gap, indicating a very high local current density that increased the overall current. The cell length had little effect on the shunting current. This can be understood by noting that the equipotential lines in the gap region varied little with cell length, and this region was the primary factor limiting

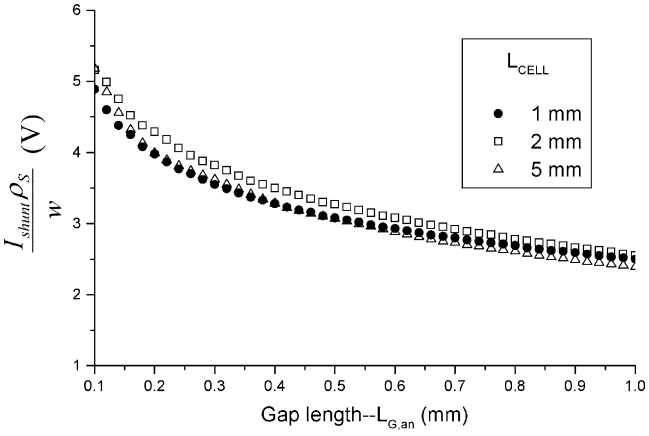

Fig. 12. Shunting current vs. gap length for various active cell lengths.

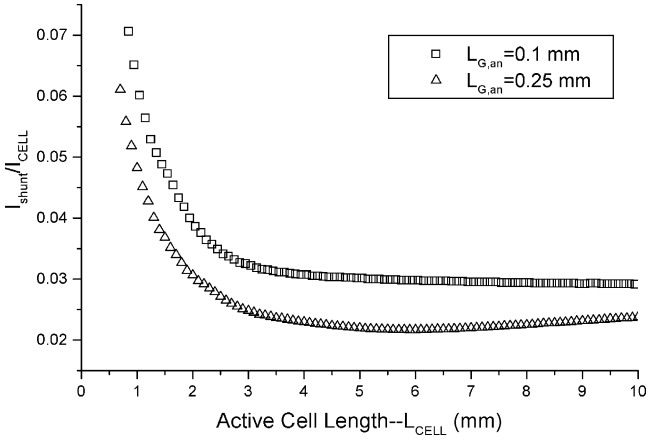

Fig. 13. Ratio of shunting current to cell current plotted vs. active cell length for gap lengths of 0.1 and 0.25 mm. Cell currents were obtained from the data plotted in Fig. 7, assuming $R_{\text{AS}} = 0.5\,\Omega\,\text{cm}^2$.

the shunting current (in the active cell length the conductive Ni–YSZ anode provided an easy short-circuit current path). The present results are for one specific support thickness; in general, the shunting current will increase with increasing support thickness.

Fig. 13 shows the ratio of I_{shunt} to I_{CELL} as a function of L_{CELL}, assuming an operating temperature of 800 °C. $L_{\text{G,an}}$ was taken to be 0.25 mm and cell performance data were the same as the $R_{\text{AS}} = 0.5\,\Omega\,\text{cm}^2$ series in Fig. 7. At $L_{\text{CELL}} \approx 6$ mm, the ratio goes through a minimum value of about 0.026 due to the increasing cell current. Below $L_{\text{CELL}} \approx 1$ mm, $I_{\text{shunt}}/I_{\text{CELL}} > 0.05$. As L_{CELL} approaches 10 mm, the ratio rises slightly because the long current path has a detrimental effect on cell performance.

Fig. 14 shows the predicted shunting current assuming $L_{\text{G,an}} = 0.4$ mm, $L_{\text{CELL}} = 1.8$ mm, and $w = 8.5$ mm. The current increases with increasing cell operating temperature. The highest value was 8.2 mA at 1000 °C, whereas the low-

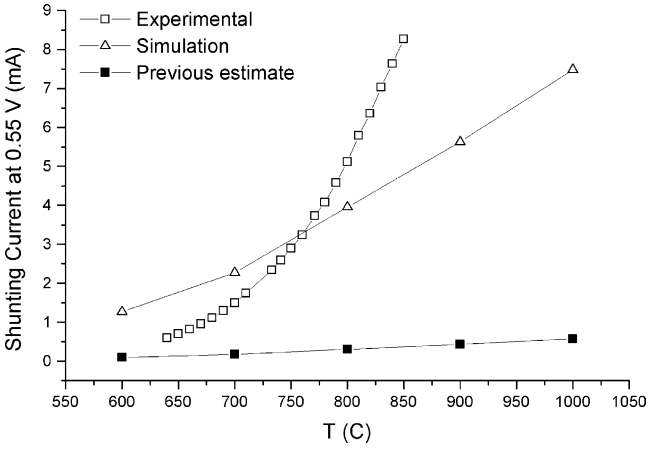

Fig. 14. Shunting current vs. temperature comparing the present calculation, a previous approximate calculation assuming a uniform field across the support [4], and an experimental measurement. For each of these, $L_{\text{G,an}} = 0.4$ mm, $L_{\text{CELL}} = 1.8$ mm, and $w = 8.5$ mm.

est value was 1.4 mA at 600 °C. At the expected operating temperature of 800 °C (a resistivity of 752 Ω cm after correction for porosity), the shunting current was calculated to be 4.3 mA, translating to at most a 5–6% degradation in MPD when considering the performance data given in Fig. 7.

An experimental check of the calculation results was obtained by making resistance measurements (in humidified hydrogen) across an array of four Ni–YSZ anodes printed onto the surface of a porous PSZ substrate. The dimensions were the same as those used in the calculation in Fig. 14. The measured current, shown in Fig. 14, increased with increasing temperature, like the calculation result, but at a faster rate. While the reason for the difference in slope is not known, there was reasonable agreement between the magnitudes of the measured and predicted shunting currents. Note that the measured values are lower than the predicted values at lower temperatures; this may be due to the effect of polarization resistance, which was not considered in the calculation. Also plotted are shunting current values calculated assuming a uniform electric field across the array repeat period Λ and an operating voltage of 0.55 V, as mentioned in our previous paper [4]. This method produced shunting current values at least a factor of 10 less than those calculated using the present method. These results illustrate the importance of operating temperature on the shunting current, originating from the temperature dependence of the PSZ resistivity. Lower temperatures are clearly desirable to minimize shunting current, assuming that the cell current does not decrease too much at the lower temperature.

4. Discussion

The above results show how the geometry of segmented-in-series SOFCs determine their performance. For cells with low area specific resistance, relatively small cell lengths and cathode sheet resistances are required to achieve high power densities, in agreement with prior predictions [4]. Otherwise, the electrolyte current is non-uniform across the length of the cells, with much of the area not contributing significantly to the cell current. The above results predict an optimum cell length by accounting for the interconnect area. Assuming typical SOFC materials properties and corresponding area-specific resistance values of $\approx$0.3–0.5 Ω cm^2, along with geometries and layer thickness characteristic of screen printing, optimal power densities were achieved for cell lengths of 1–2 mm. For the 10-mm-long cells that have traditionally been used in segmented-in-series SOFCs, power densities are much lower unless very thick (>200 μm) cathodes or more conductive ($\gg$100 S cm^{-1}) cathode materials are employed.

Interconnect resistances for segmented-in-series SOFCs did not become a limiting factor, despite the relatively low conductivity ($\approx$1 S cm^{-1}) assumed for typical ceramic interconnects, unless the interconnect length was $\leq$0.1 mm ($\leq$5% of the cell area). This is primarily due to the segmented-in-series geometry, in which the thin ($\approx$20 μm) interconnect is sandwiched between more conductive anode and cathode layers. Since standard materials such as $LaCrO_3$ sinter poorly, thin and dense ceramic interconnect layers are difficult to produce [11]. In addition, the interconnect should be co-sintered with the support, anode, and electrolyte layer, providing further constraints on sintering conditions to avoid possible reactions that could form resistive interfacial phases. Nonetheless, dense $LaCrO_3$-based interconnect layers have been reported using sintering aids [12].

The effects of shunting current were evaluated for the case of zirconia-based supports, which are convenient for SS-SOFCs because of the good chemical stability and thermal expansion match with SOFC materials. For reasonable area-specific resistance, cell length, and operating temperature $\leq$800 °C, the shunting current will not substantially affect overall power density. However, shunting current may become important for higher temperatures and for cell repeat periods < 1.2 mm, where the shunting current comprises $\geq$ 5% of the cell current.

While it is inevitable that comparisons will be made between area-specific power densities for different stack designs, volumetric power density and cost per kW are the more relevant quantities. For this, the different stack geometries must be considered. While these considerations are beyond the scope of the present work, a few qualitative remarks can be made regarding how to meaningfully compare the present power densities with planar SOFCs. First, SS-SOFC power densities calculated here include interconnect and current collection losses, such that they should be compared with planar SOFC *stack* results, rather than single cells. Note that the power densities predicted above for SS-SOFCs are generally lower than for planar single cells, which are typically > 1 W cm^{-2} at 800 °C, but are similar to those for planar SOFC stacks (typically $\approx$ 0.5 W cm^{-2}). Second, the power densities in Fig. 8 include both cell and interconnect areas in the calculation. In contrast, power density calculations for planar stacks generally do not include interconnect area. Thus, a more appropriate comparison would be to use the power density calculated using only active cell area, e.g. Fig. 7, evaluated at an appropriate cell length.

5. Summary and conclusions

Calculations were done to predict (a) the electrical behavior of segmented-in-series SOFCs based on their geometry and components' sheet resistances, and (b) the shunting current flowing between cells through the porous substrate. Calculations were made using array geometries reflecting the capabilities of screen printing and conductivities typical of SOFC materials. For a gap length of 0.25 mm and an assumed operating temperature of 800 °C, the shunting current through the substrate was estimated to be $\leq$6% of typical cell currents. For area specific cell resistances of 0.2, 0.3, 0.5, and 1.0 Ω cm^2, the optimum maximum power densities occurred from 1.05–1.9 cm for $L_{G,an} = L_{G,ca} = L_I = 0.25$ mm

and 0.8–1.45 cm for $L_{G,an} = L_{G,ca} = L_I = 0.1$ mm. The calculations can be used to design and optimize SS-SOFCs for a given materials set, operating condition, and processing technique. For typical SOFC materials and layer thicknesses typically obtained by screen printing, reducing the active cell length from 10 mm to 1–3 mm should result in a significant improvement in power density.

Acknowledgments

The authors gratefully acknowledge financial support from the US Department of Energy Coal Research Program, and National Defense Science and Engineering Graduate Fellowship support for T.S. Lai.

Appendix A. Definitions for symbols

Symbol	Meaning
dI_{an}	Change in anode current in length element dx
dI_{ca}	Change in cathode current in length element dx
dV_{an}	Voltage drop across anode in length element dx
dV_{ca}	Voltage drop across cathode in length element dx
I_{an}	Current flowing through anode
I_{ca}	Current flowing through cathode
I_{CELL}	Cell current
I_{shunt}	Shunting current
J_{el}	Flux of electrons thrown electrolyte
Λ	Repeat period of array
L	Anode length plus half of anode gap length
L_{CELL}	Cell length
$L_{G,an}$	Gap length between anodes
$L_{G,ca}$	Gap length between cathodes
L_I	Length of interconnect
ρ_{an}	Resistivity of anode
ρ_{ca}	Resistivity of cathode
$R_{an/el}$	Resistance of anode/electrolyte interlace
R_{AS}	Area specific resistance of cell (excluding electrodes), $R_{el} + R_{an/el} + R_{ca/el}$
$R_{ca/el}$	Resistance of cathode/electrolyte interlace
R_{el}	Resistance of electrolyte
t_{an}	Thickness of anode
t_{ca}	Thickness of cathode
t_{el}	Electrolyte thickness
t_I	Interconnect thickness
t_S	Substrate thickness
V_{an}	Voltage of anode (relative to 0)
V_{ca}	Voltage of cathode (relative to 0)
V_o	Cell operating voltage
V_{OC}	Open circuit voltage of cell
w	Cell width
x	Position along cell length
y	Distance from substrate surface
z	Direction perpendicular to xy plane

References

[1] A.O. Isenberg, Solid State Ionics 3–4 (1981) 431–437.
[2] F.J. Gardner, M.J. Day, N.P. Brandon, M.N. Pashley, M. Cassidy, J. Power Sources 86 (2000) 122–129.
[3] P. Costamagna, A. Selimovic, M. Del Borghi, G. Agnew, Chem. Eng. J. 102 (2004) 61–69.
[4] T.S. Lai, J. Liu, S.A. Barnett, Electrochem. Solid-State Lett. 7 (4) (2004) A78–A81.
[5] Matlab, Version 6.5, The MathWorks, Inc., 2002.
[6] E.M. Pugh, E.W. Pugh, Principles of Electricity and Magnetism, Addison-Wesley, Reading, MA, 1970, Section 4–6.
[7] E.M. Pugh, E.W. Pugh, Principles of Electricity and Magnetism, Addison-Wesley, Reading, MA, 1970, Section 6–7.
[8] N.Q. Minh, J. Am. Ceram. Soc. 76 (3) (1993) 563–588.
[9] S.J. Skinner, Int. J. Inorg. Mater. 3 (2) (2001) 113–121.
[10] S.P.S. Badwal, M.V. Swain, J. Mater. Sci. Lett. 4 (4) (1985) 487–489.
[11] J.W. Fergus, Solid State Ionics 171 (1–2) (2004) 1–15.
[12] S.P. Simner, J.S. Hardy, J.W. Stevenson, T.R. Armstrong, Solid State Ionics 128 (2000) 53–63.